Manufacturing and assembly of an all-glass OCT microendoscope

To cite this article: Yanis Taege *et al* 2021 *J. Micromech. Microeng.* **31** 125005

View the article online for updates and enhancements.

Manufacturing and assembly of an all-glass OCT microendoscope

Yanis Taege* , **Gerardo González-Cerdas** , **Felix Jund** , **Hans Zappe** and **Çağlar Ataman***

Gisela and Erwin Sick Laboratory for Micro-Optics, Department of Microsystems Engineering, University of Freiburg, Freiburg, Germany

E-mail: yanis.taege@imtek.uni-freiburg.de

Abstract

We present a forward-looking, fiber-scanning endomicroscope designed for optical coherence tomography (OCT) and OCT-Angiography (OCT-A) imaging through the working channel of commercial gastrointestinal endoscopes and cystoscopes. 3.4 mm in outer diameter and 11.9 mm in length, the probe is capable of high-resolution volumetric imaging with a field-of-view of up to 2.6 mm and an imaging depth of up to 1.5 mm at a lateral resolution of 19 μm. A high-precision lens mount fabricated in fused silica using selective laser-induced etching (SLE) allows the tailoring of the optical performance for different imaging requirements. A glass structure fabricated by the same method encapsulates the optical and mechanical components, providing ease of assembly and alignment accuracy. The concept can be adapted to high resolution OCT/-A imaging of various organs, particularly in the gastrointestinal tract and bladder.

Keywords: microendoscopy, optical coherence tomography, endoscopy, selective laser-induced etching

(Some figures may appear in colour only in the online journal)

1. Introduction

Optical coherence tomography (OCT) is a scanned-imaging technique [1] that allows non-invasive cross-sectional visualization of tissue volumes, with an isotropic resolution in the 2–40 μm range [2]. It is based on interferometric detection of low-coherence or wavelength-swept infrared light backscattered from the tissue [3], producing a depth-map of the refractive index variations in the axial direction. Lateral scanning of the beam allows acquisition of cross-sectional images. In addition to structural information, its functional extensions provide angiography (OCT-A) or elastography [4] imaging as

well. Due to this versatility, endoscopic implementations of OCT are instrumental in the attempts to attain specificity and selectivity comparable to traditional biopsy via *in vivo* imaging [5]. However, there are a number of challenges impeding the endoscopic implementations of OCT. These are

- the development of scanning engines tailored for the specifications of the OCT system,
- minimization of the length and diameter of the probe for compatibility with flexible endoscopy,
- providing optimal resolution, i.e. the number of resolvable spots in the field-of-view (FOV) within the available clear aperture,
- and an effective control of back-reflections to enhance image SNR.

State-of-the-art OCT systems use swept-source lasers with A-scan rates between 100 and 1000 KHz [6]. MEMS scanning mirrors, which are commonly used for confocal or

---

multi-photon endomicroscopes, have been implemented for endoscopic OCT instruments [7–10], but can be too fast to provide sufficient lateral sampling due to the limited A-scan rate. Furthermore, forward-looking imaging with such mirrors requires beam folding, which leads to larger, more complicated systems [11–13]. Fiber scanners can address this shortcoming by allowing a reduction of the resonance frequency as desired via the cantilever length or tip weights [14]. Particularly compact scanners can be realized using beam-shaping optics at the tip of the fiber cantilever [15–18].

We discuss here a novel approach for the implementation of OCT endomicroscopy using glass micromachining based on selective laser-induced etching (SLE) [19] that addresses all major challenges listed above. SLE is a laser machining technology that combines femtosecond laser-writing with wet-etching to manufacture transparent free-form structures with a micrometer-scale precision [20]. Through extensive use of SLE for both mechanical and optical features of this probe, we were able to realize a lens-on-fiber scanner, encapsulation that acts as a precision micro-assembly platform, and auxiliary micro-assembly tools for robust and repeatable manufacturing. Combining the lens-on-fiber scanner with a non-telecentric design allows for precision tailoring of the opto-mechanical specifications based on the target application. The manufactured probe provides a non-telecentric FOV of up to 2.6 mm for operation in contact mode with 19 μm resolution.

2. Probe design

Since the optical and mechanical properties of a fiber-scanner are inherently coupled, sections 2.2 and 2.3 will discuss the adaptation of both to the design requirements, while their integration into a glass platform will be described in section 2.4.

2.1. Design requirements

The target specifications for the OCT/-A probe are set considering use in clinical cystoscopy equipment. Operation in a working channel implies a maximum outer diameter of 2.3–4 mm [21, 22] including encapsulation. In terms of optical performance, a lateral resolution between 10 and 20 μm is required to resolve features of the microvasculature [23]. A depth-of-field (DOF), which is a measure for the axial extent of the imaged volume, of at least one millimeter is a favorable trade-off with the lateral resolution. To image a significant portion of the microvasculature network, maximization of the FOV to the mechanical limits of the probe is another requirement.

2.2. Optical design

One of the most promising approaches for miniaturized scanning is fiber-based [24], which relies on resonant excitation of a fiber cantilever. These fiber-scanner implementations have different limitations: use of bare fibers can provide a large
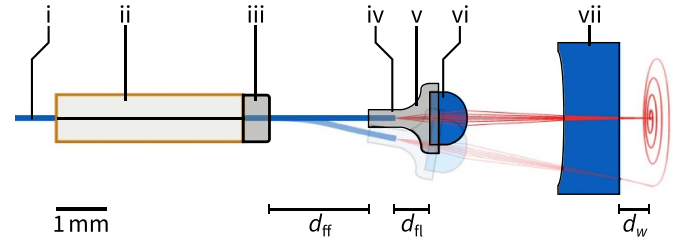

Figure 1. Schematic of the optical design of the non-telecentric scan engine. A fiber (i) is connected to a tubular piezo actuator (ii) using an alignment ring (iii). The interface of the fiber (iv) is connected to a fiber-lens connector (v), in which a plano-convex lens is mounted (vi). The distal end of the optical assembly is a plano-concave lens (vii). Important opto-mechanical parameters are the free fiber distance d_{ff}, the fiber-lens distance d_{fl} and the working distance d_{w}.

FOV, but requires long probe heads due to the light tip weight [24, 25]; a Fourier-plane implementation precisely defines an imaged cylinder, but can only provide a limited resolution and FOV due to the aperture restrictions [26]; and assemblies which use a GRIN lens at the cantilever tip significantly shorten the probe heads, but are limited in optical design versatility [15].

Here, we propose and demonstrate a non-telecentric design which is able to overcome some of those limitations [17]. The design is illustrated in figure 1. It features a plano-convex lens (67 423, Edmund Optics Ltd), which focuses a beam from a single-mode fiber (SM980G80, Thorlabs Inc) towards a plano-concave lens (67 979, Edmund Optics Ltd). Both lenses have an anti-reflection coating for the NIR-II range, minimizing back-reflections. To allow in-contact operation, the working distance d_{w}, i.e. the distance from the plano-concave lens to the focal point, was set to 0.5 mm in water.

Part of the versatility of this system arises from use of the laser-machined fiber-lens connector, which holds the fiber and convex lens in place. Adjustment of the distance between lens and fiber, d_{fl}, allows the tuning of the optical performance to the needs of the specific application. While keeping the working distance of the probe fixed, the system's numerical aperture increases with d_{fl}, since the distance between both lenses is reduced. On one hand, this increase results in an increase in lateral resolution Δr and a decrease in optical system length l_{sys} (fiber facet to distal end); however, it also shortens DOF.

To numerically investigate the imaging performance, optical simulations using a commercial ray-tracing software (OpticStudio 20.1, Zemax) were performed. While the influence of d_{fl} on NA and optical system length l_{sys} were taken from the ray-tracing model, axial resolution Δx was derived from the Rayleigh contrast of the modulation transfer function (MTF). Since illumination and collection is performed by the same imaging system, the imaging MTF is the autocorrelation of the calculated system MTF. The DOF was calculated according to

$$\text{DOF} = 2z_{r} = 2\frac{n\lambda_{0}}{\pi\text{NA}^{2}} \qquad (1)$$
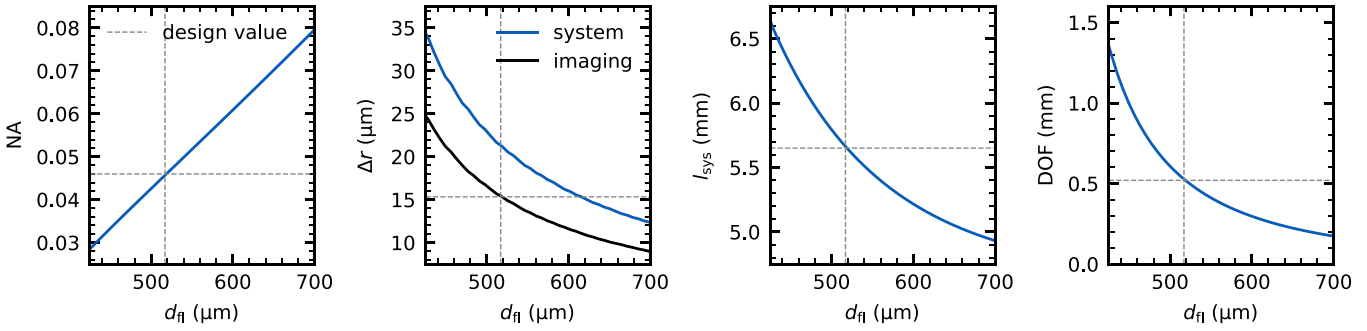
Figure 2. Simulated optical performance including numerical aperture (NA), lateral resolution Δr for illumination (system) and imaging, optical system length l and depth-of-field DOF as a function of the fiber-lens distance d_{fl}. To achieve an imaging depth of 1.5 mm, the optimal length was taken as $d_{\mathrm{fl}} = 517\ \mu\mathrm{m}$, resulting in $\Delta r_i = 15.2\ \mu\mathrm{m}$, NA = 0.046 and an optical system length of 5.65 mm.

where z_r is the Rayleigh range, $n = 1.33$ is the refractive index of water and $\lambda_0 = 1.3\ \mu\mathrm{m}$ is the central operation wavelength.

As indicated by figure 2, with an increase of d_{fl} of only 200 μm the numerical aperture can be doubled from 0.04 to 0.08. At the same time, the length of the optical system decreases from 5.7 to 4.9 mm, which places it within the acceptable range for both flexible and rigid endoscopic probes. To achieve a total depth of field of at least 1 mm, a fiber-lens distance of 517 μm was determined. This decision is a compromise with a lateral resolution of 22.5 μm and 15.1 μm for system and imaging, respectively, with an NA of 0.046 that still allows imaging of microvasculature and keeps the optical system at a length below 6 mm.

2.3. Mechanical design

Assuming a laser sweep rate $f_s = 350$ kHz [27] and a FOV as large as the aperture of 2.7 mm, the distance Δd sampled by the beam at the outermost edge of the FOV is

$$\Delta d = \pi \cdot \frac{f_r}{f_s} \cdot \mathrm{FOV} \qquad (2)$$

where f_r denotes the resonance frequency of the fiber scanner. In order to fulfill the Nyquist criterion, Δd needs to be half of the lateral resolution, leading to a maximal resonance frequency of 312 Hz.

The free fiber distance d_{ff} between the alignment ring and the lens connector allows adjustment of the resonance frequency of the scanning unit. This mechanical system was simulated using a finite-element analysis (Comsol 5.4, COMSOL Multiphysics GmbH). While the actuator was modeled as a radially polarized tube of PIC151 consisting of four independent electrodes (PI Ceramic GmbH), the alignment ring, and the fiber-lens connector were modeled using the mechanical properties of fused-silica parts, and the lens those of N-LASF9.

A modal analysis in the range from 1 to 3 mm of fiber length l was performed and the results fitted by an analytical resonant beam theory model for the resonant frequency [14], namely
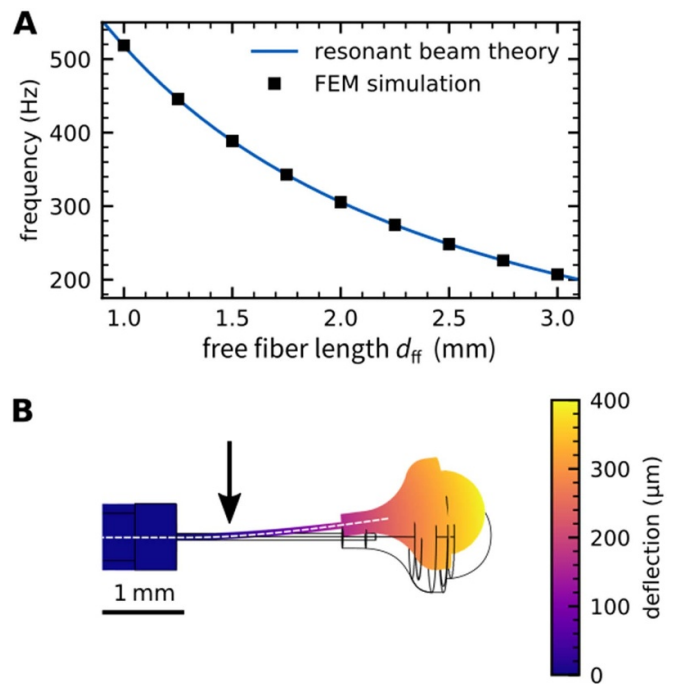
$$f_r = \sqrt{\frac{K}{m(l - l_0)^3}}, \qquad (3)$$

Figure 3. Results of the FEM simulation. (A) Simulated values of resonance frequency compared with analytical resonant beam theory. The center-of-mass is located 122 μm in front of the fiber tip. (B) Excited mode shape in terms of deflection for a free fiber length of 2 mm. Solid dark lines indicate the unexcited position. The arrow indicates the estimated deflection point used for the FOV estimation in section 3.4, and the white dashed line the mode shaped used for the design of the scanning inlet (figure 4).

where K denotes the spring constant of the fiber, and m and l_0 denote the effective mass at the cantilever tip and the distance from the fixed end to the center of mass, respectively. From this model, we find that a resonance frequency of 306 Hz, which is slightly below the maximal scanning frequency, is achieved for a free fiber length of 2 mm as seen in figure 3.

However, such design freedom could only be exploited if a high accuracy of d_{fl} was achieved. Even under the conservative assumption of $\pm 15\ \mu$m in SLE tolerancing, a d_{fl} between 480 and 540 μm would fulfil the resolution requirement imposed by cystoscopic angiography. This critical axial alignment step is thus intrinsically achieved by the fiber-lens
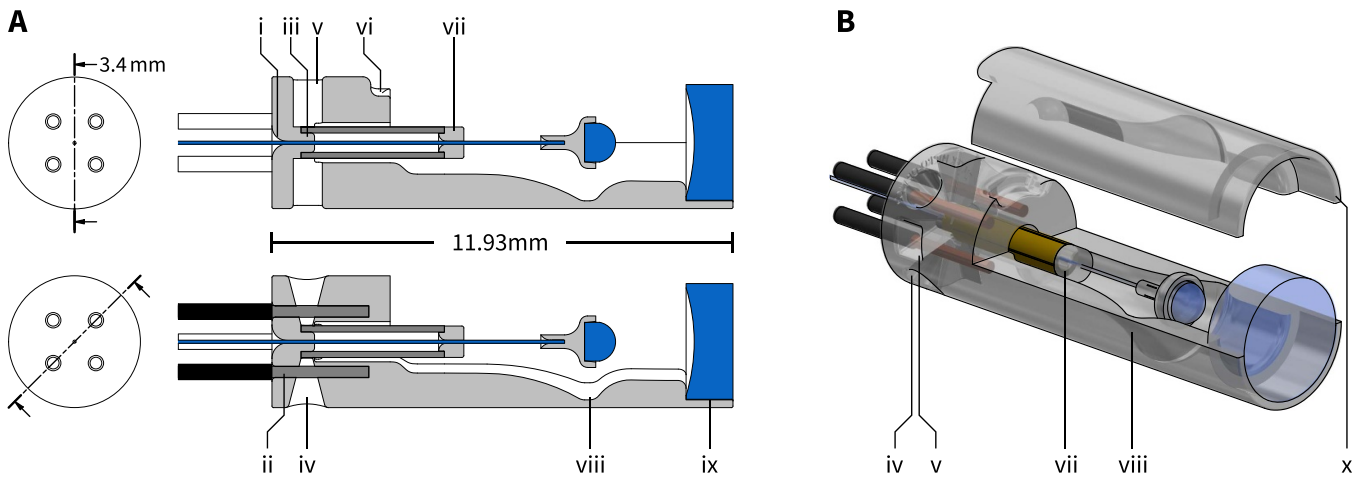
Figure 4. Design of the glass housing. (A) Section views of the glass housing at two different angles, providing support to all opto-mechanical components. (B) 3D-render of the glass housing with the components mounted and its cap lifted. Legend: fiber funnel (i), wire channels (ii), piezo mount (iii), conical connectorization hole (iv), electrode window (v), cap inlet (vi), alignment ring connecting piezo and fiber (vii), a scanning inlet (viii), distal mount for the plano-concave lens (ix) and cap (x).

connector. Another problem that is inherently solved with this assembly is the optical coupling between fiber and lens, which is overcome by using an index-matched, UV-curable glue (Loctite 3301, Henkel AG & Co. KGaA) at this interface, as well as at the one between connector and lens.

2.4. Platform design

The design of the housing took the advantage of SLE in creating hollow free-form structures into account, which allowed to include nearly all components in a single piece of glass, which is shown in figure 4. At its proximal end the housing features a mount for the piezoelectric tube (PT) which aligns the scanning unit to the optical fiber and the center of the probe. For two-dimensional scanning, all four external electrodes of the PT need to be connectorized manually. Holes for applying conductive epoxy and windows for checking the electrode alignment are included at the proximal end. Each of the holes is intercepted by a channel for holding the wires in place.

A mount for the plano-concave lens is placed at the distal end of the probe. Since an outer wall thickness below 200 μm can result in mechanical instability, this part poses the limiting factor on the probe's outer diameter.

Another particular feature is the inlet for scanning. As a thicker glass housing provides more mechanical stability, the highest infill ratio should be used when designing rigid parts, particularly along the main axis. However, it should allow the scanning unit to use the full aperture size of the distal lens. To achieve that, the mode shape (figure 3(B)) is carved along the housing's axis (scanning inlet, viii in figure 4) to provide room for a maximum scanning angle with highest rigidity.

The final dimensions of the housing add up to 11.93 mm in length and 3.4 mm in diameter. The smallest hollow features are channels for the stripped fiber with a diameter of 80 μm.

2.4.1. Multi-axes, free-form assembly platform.

As described in the previous section, all components mounted

directly on or into the housing are intrinsically aligned to the extent of the SLE's manufacturing tolerances. The alignment of the oscillating fiber and lens, however, requires to be taken care of separately. In our previous work, this has been achieved by sliding a two-dimensional alignment structure, in which all optical components are placed, into the housing [18]. After fixing all components in place, the fiber assembly was slightly lifted and subsequently removed. Due to the large diameter of the fiber-lens connector this procedure is not applicable to this design, which is why a multi-axes alignment platform (AP) was additionally manufactured.

Multi-axes refers to the fact that it does not only align the lens connector assembly along the optical axis, but also laterally. This is crucial, as misalignment at this point translates directly to the scanning behavior, and thus into distortion in he scanning behavior.

The AP accomplishes that by having a nozzle with the exact negative imprint of lens and lens connector, which is shown in figure 5. Both are held in place by an external vacuum, which is connected through channels in the back-end of the AP. Its main body allows the insertion of the probe with the piezo mounted, but the fiber being movable. After pushing the fiber through the probe, the alignment ring and the proximal end of the lens connector, the entire assembly can be glued in the aligned state.

The remaining steps consist of mounting the plano-concave lens and closing the probe using a cover.

3. Materials and methods

3.1. Manufacturing of fused-silica parts

All parts manufactured using SLE were semi-automatically pre-processed (Rhino 6, Robert McNeel & Associates) before writing them into fused-silica substrates (Toppan Inc.) using a commercial laser microscanner (LightFab GmbH). They were subsequently etched in a potassium hydroxide (KOH)
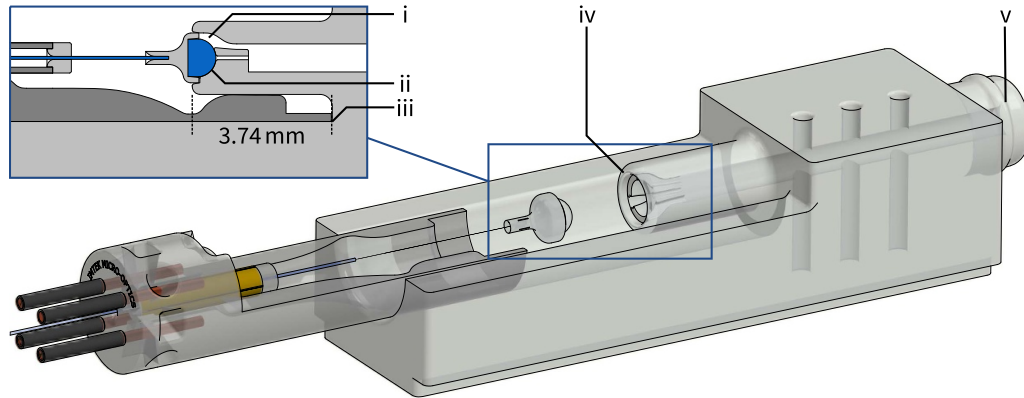
Figure 5. Overview of the multi-axis alignment platform (AP) and procedure. The main feature of the AP is its ability to laterally align lens and lens connector using vacuum channels (i) in a negative imprint (ii). Axial alignment is achieved by inserting the probe housing into the alignment structure to a stop (iii), such that the nozzle's tip (iv) is at the correct axial position. An external vaccuum is connected at the back end (v) of the AP. After inserting the fiber through the back of the probe all scanning components can be fixed into place using UV-curable glue.

solution with a concentration of 8 mol l^{-1} at a temperature of $(78 \pm 2)\,°C$. Depending on their dimensions and features this process took 8–48 h.

3.2. OCT-setup

The optical source was an akinetic swept-source laser (SLE-101, Insight Photonic Solutions Inc), which operates at a central wavelength of 1.3 μm. The sweep rate was 173 kHz and the bandwidth 90 nm. Synchronized operation of the laser, the detector and the power amplifier was ensured with an FPGA. Signal detection was performed by a balanced detector (BPD-1, Insight Photonic Solutions Inc).

3.3. Mechanical characterization

The mechanical performance of the probe was evaluated by recording the deflection of the beam on a position sensitive detector (PSD; Spotana-9L, Duma Optronics Ltd). As a first step, the resonance frequencies of both the piezo's axes were determined by a frequency sweep over the designed range (290–310 Hz) with a maximum voltage of 5 V. With an offset of $+2$ Hz to the resonance frequency, both electrodes were driven up to the maximum voltage of 75 V while keeping the scan pattern as circular as possible. The voltage and frequency of a stable, circular scan pattern were then used as an operating point of the specific probe for all subsequent measurements.

3.4. Optical characterization

The system's optical performance was quantified by means of the FOV, the MTF and the DOF, as well as the reduction of back-reflections during assembly.

Straightforward estimation of the FOV by placing the PSD at the working distance of the probe is not necessarily accurate in the case of a non-telecentric probe. Since the FOV scales with distance to the probe, it is favorable to estimate the *opening* angle α for a specific operating point. This way the conical rather than tubular volume, which is imaged by the

probe, can be estimated. To achieve that, the scan pattern was recorded by the PSD at four different axial locations behind the probe. By linearly fitting the outermost edge of the scan pattern with distance as an independent variable, α can be deduced. An estimation of the FOV at the focal point can then be obtained by

$$\text{FOV} = 2d_{\text{f}} \tan \alpha \qquad (4)$$

where $d_{\text{f}} \approx 6.3$ mm is the distance between the deflection point and the focus of the probe. The latter was estimated using the results of the FEM simulations (see section 2.3).

To deduce the MTF, we obtained the edge spread function (ESF) by moving the focus of the non-scanning probe over a sharp chromium edge using an *xy*-stage [28]. The ESF was estimated by fitting a logistic function to the measured data using a non-linear least squares algorithm [29, Scipy 1.6.1]. The line spread function, with which one approximates the point spread function, is calculated analytically using the derivative of the fitted ESF. In a final step, the fast-Fourier transform of the LSF yielded the MTF. The axial resolution of the system's imaging capabilities was estimated using the Rayleigh contrast limit of 0.159 applied to the MTF.

To estimate the DOF, the sample arm of the OCT setup was connected to an optical power meter (PM100D, Thorlabs Inc) instead of the balanced photodetector. After maximizing the reflected signal from a mirror in front of the probe head, the probe was moved axially away from the mirror while recording the change in power. The Rayleigh range was estimated by a non-linear least-squares fit of the hyperbolic axial behaviour of a Gaussian beam from which the DOF was calculated according to equation (1).

The reduction of back-reflections using the index-matched resin was estimated during assembly with a similar setup as for the DOF measurements. The only difference was a change in the source, which was an SLED (SLED 319, Covega). The back-reflected power was recorded without glue, with glue and after curing.
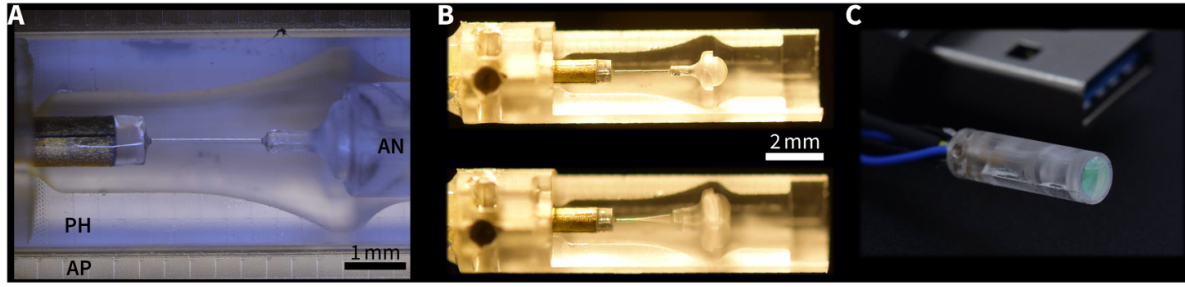
Figure 6. Images of the assembly process of the probe. (A) Critical alignment step of the lens and lens connector to the optical fiber. Lens and lens connector are held by the alignment nozzle (AN) of the alignment platform. The probe housing (PH) is temporarily fixed to the AP during this procedure. (B) Finished scanning unit of the probe with the lens centered. During resonant actuation of the piezoelectric tube the scanning behavior can be directly observed, shown in the bottom image (exposure time: 17 ms). (C) Assembled probe and enclosed probe. For size reference, a Type A USB connector has been placed in the background.

3.5. Optical coherence tomography

OCT was performed on the finger tip of a healthy volunteer (male, 28 y old). Informed written consent was obtained prior to the experiment, and the study was in agreement with the tenets of the Declaration of Helsinki and approved by the institutional ethics committee. The scan, which took 0.5 s, was performed on the left index finger.

4. Results

Figure 6(A) gives an overview of all scanning components just after application of the index-matching glue. While the lens connector is laterally and axially fixed by the AP, the alignment ring can still be adjusted. The assembled components are shown in figure 6(B), where also the scanning capability through actuation is visualized. After mounting the plano-concave lens at the distal end of the probe the probe is closed by its cover, resulting in the final probe head (figure 6(C)).

4.1. Mechanical performance

The frequency response of the probe, shown in figure 7(A), revealed a resonance frequency of (302.6 ± 0.1) Hz and a Q-factor of 99 ± 2, which closely matches the simulated value of 306 Hz. This is true for both axes of the probe, and underlines the precise lateral alignment of the scanning unit.

A stable operation point was found at 306 Hz with an opening frequency of the spiral of 0.5 Hz and a maximal electrode voltage of 75 V on one axis and 69 V on the other. Figure 7(B) shows the quasi-circular pattern, in which the deviation in deflection on both axes was only differing by 6.5%.

4.2. Optical performance

The imaging MTF derived from the edge-spread-function revealed a lateral resolution of 19 μm according to the Rayleigh criterion in figure 8, which is 23% larger than the simulated value. Using the non-telecentric FOV calibration, an opening angle of $(11.8 \pm 0.1)°$ was determined, which
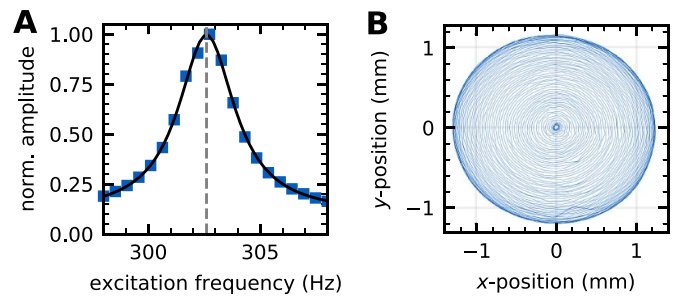

Figure 7. Results of the mechanical performance of the assembled OCT-probe. (A) Bode plot showing the frequency response of the scanning unit. The resonance frequency was determined to be (302 ± 1) Hz at a quality factor of 99 ± 2. (B) Scan pattern of the probe at a *x*- and *y*-voltage of 69/75 V, respectively, with an excitation frequency of 306 Hz. The opening frequency of the spiral was 0.5 Hz. To improve visualization, only 1% of all scanned points are plotted.

corresponds to a FOV of (2.6 ± 0.1) mm in water. Therefore the space-bandwith-product SBP of the probe is [30]

$$\text{SBP} = \frac{\text{FOV}}{2\,\Delta r} = 68 \pm 2. \qquad (5)$$

Estimation of the Rayleigh range revealed a DOF of (1.06 ± 0.02) mm which is twice the designed value.

Power measurements during assembly showed a drop in back-reflections by 91% from 558 ppm to 51 ppm when applying the index-matched glue to the fiber-lens connector interface. After curing, this ratio dropped by another 2% to 41 ppm.

4.3. Optical coherence tomography

Images generated of three-dimensional volumes of a human fingertip placed at the front of the probe revealed several anatomical features. To facilitate visualization, figure 9 shows a B-scan at the outermost edge of the FOV alongside the 3D-rendered OCT volume. The location of the scan is denoted by a red circle. In the image, one can identify the epidermis with a thickness of around half a millimeter through the strongest reflection in the image, as well as the dermis. The rendered
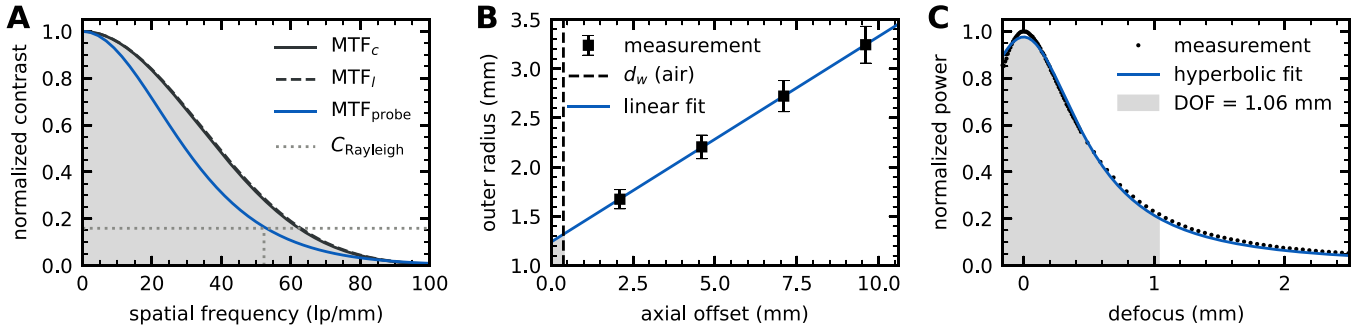
Figure 8. Determined optical performance of the OCT probe. (A) Derived modulation transfer function MTF_{probe} alongside the simulated MTFs at no deflection and maximum lateral deflection (MTF_c and MTF_l, respectively). The measured MTF revealed a resolution $\Delta r = 19\,\mu m$ according to the Rayleigh criterion. (B) Determination of the field-of-view (FOV) by axially moving the probe away from the PSD. The fit revealed an opening angle of $(11.8 \pm 0.1)°$, which corresponds to a FOV of (2.6 ± 0.1) mm. (C) Determination of the depth-of-field (DOF) by moving a power detector through the probe's focus, revealing a DOF of (1.06 ± 0.02) mm.
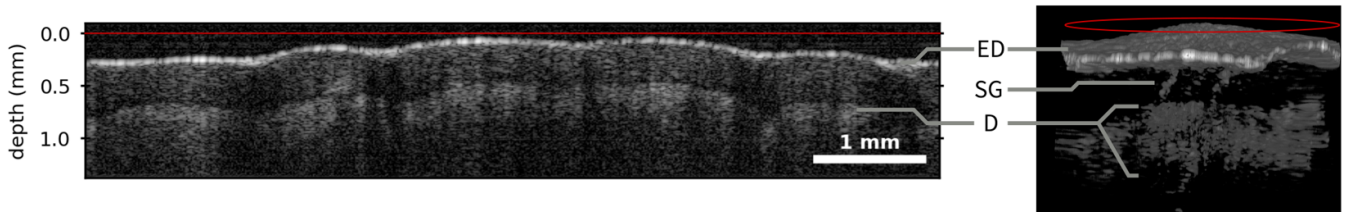

Figure 9. OCT image of a human fingertip. A B-scan through the outermost edge of the FOV is shown alongside the 3D-render of the entire volume. The red line and red circle mark the approximate location of the B-Scan. The epidermis (ED) can be identified as the strongest reflection just after the window. Further identifiable anatomical features are the dermis (D) at a depth of around 0.5 mm as well as sweat glands (SG).

volume also visualizes the sweat glands which diagonally stretch through the acquired volume. In the axial direction the signal drops off at about 1.5 mm, which supports the DOF measurements.

5. Discussion and conclusions

The combination of an integrated glass housing together with an alignment platform demonstrated the capability of SLE as a technology platform for excellent alignment of a complex micro-optical system.

Precise lateral alignment was confirmed by the symmetrical scan pattern, which was the most critical step in the assembly process. This step was facilitated making use of an alignment platform manufactured using SLE, which also enabled axial alignment. The precision of the latter was verified by both the resonance sweep closely matching the predicted resonance frequency from FEM simulations, as well as its DOF analysis.

By manufacturing a fiber-lens connector we have been able to freely tailor the optical performance to the application needs of this OCT probe. This design made the optical properties, namely NA and therefore the resulting lateral resolution and DOF, very sensitive to the distance between fiber and lens d_{fl}. The measured lateral resolution of 19.1 μm is lower than the designed value of 15.1 μm, which points to a reduced d_{fl} of about 30 μm. The measured DOF, which is larger than the simulated value, supports this hypothesis since a reduction in

d_{fl} also causes a reduction in NA. A possible reason for this is over-etching of the custom lens holder, which is caused by a finite selectivity of the SLE process. This deviation is, however, challenging to correct, since the surface roughness at the interface is in the range of 6 μm. This roughness is compensated in terms of optical surface matching with the UV-curable glue, but it still limits the range of adjustment of d_{fl}. Nonetheless these tolerances have been accounted for during the design process by choosing d_{fl} such that the lateral resolution is within specification for the application needs. The probe was thus able to deliver images with structural information of the required resolution throughout the FOV.

5.1. Conclusions

To our knowledge, the most significant advance in this design is the large FOV and SBP with respect to the size of the probe. Due to the relatively large weight at the cantilever tip, the opening angle of the probe allows a FOV almost as large as the largest aperture size. Relating that to the probe's diameter, we achieved a diameter coverage $c_d = FOV/d_{probe}$ of 76%. Other scanning probes either provide a coverage below 50% [15, 26] or are significantly longer [25].

Another advantage of the non-telecentric design of the probe plays a significant role when translating it to non-contact operation. As the FOV scales linearly with the working distance, an adapted optical design would allow a coverage several times as large as the probe's diameter. The opening

angle determines the maximum enhancement possible, and the design is likely at the maximum limit for this parameter. However, non-contact operation requires either tissue fixation or fast acquisition to avoid motion artifacts.

Another application area is OCT-A, which is enabled without any further modifications of the implementation discussed here. The small FOV of most forward-looking probes has limited the application of OCT-A, a limitation which can be overcome with this design. To push OCT-A to its limits, the probe head could yet be adapted in terms of cantilever frequency and optical resolution.

In summary we have presented SLE as an enabling technology platform to manufacture and assist in the assembly of a high performance OCT microendoscope which provides both high resolution and a large FOV. With its small diameter this development significantly extends the limits of large-area OCT-imaging through an endoscope's working channel. Due to the compact nature of the design, applications may not only be limited to rigid endoscopes but also include those with flexible channels.

Data availability statement

The data that support the findings of this study are available upon reasonable request from the authors.

Acknowledgments

ORCID iDs

Yanis Taege https://orcid.org/0000-0002-0390-2582
Gerardo González-Cerdas https://orcid.org/0000-0002-7096-023X
Felix Jund https://orcid.org/0000-0003-1706-1726
Hans Zappe https://orcid.org/0000-0003-4603-8613
Çağlar Ataman https://orcid.org/0000-0002-6280-8465

References

[1] Lee C M, Engelbrecht C J, Soper T D, Helmchen F and Seibel E J 2010 *J. Biophoton.* **3** 385–407

[2] Drexler W and Fujimoto J G 2013 *Optical Coherence Tomography* 2nd edn (Switzerland: Springer)

[3] Huang D *et al* 1991 *Science* **254** 1178–81

[4] Kim J, Brown W, Maher J R, Levinson H and Wax A 2015 Functional optical coherence tomography: principles and progress *Phys. Med. Biol.* **60** R211–37

[5] Sung H H, Scherr D S, Slaton J, Liu H, Feeny K L, Lingley-Papadopoulos C, Gearheart J, Zara J M and Lerner S P 2021 *Urol. Oncol.* **39** 434.e23–434.e29

[6] Drexler W, Liu M, Kumar A, Kamali T, Unterhuber A and Leitgeb R A 2014 *J. Biomed. Opt.* **19** 071412

[7] Jung W, McCormick D T, Zhang J, Wang L, Tien N C and Chen Z 2006 *Appl. Phys. Lett.* **88** 163901

[8] Kim K H, Park B H, Maguluri G N, Lee T W, Rogomentich F J, Bancu M G, Bouma B E, de Boer J F and Bernstein J J 2007 *Opt. Express* **15** 18130

[9] Sun J, Guo S, Wu L, Liu L, Choe S W, Sorg B S and Xie H 2010 *Opt. Express* **18** 12065

[10] Wang D, Fu L, Wang X, Gong Z, Samuelson S, Duan C, Jia H, Ma J S and Xie H 2013 *J. Biomed. Opt.* **18** 086005

[11] Kumar K, Condit J C, McElroy A, Kemp N J, Hoshino K, Milner T E and Zhang X 2008 *J. Opt. A: Pure Appl. Opt.* **10** 44013–20

[12] Lu C D *et al* 2014 *Biomed. Opt. Express* **5** 293

[13] Kim S, Crose M, Eldridge W J, Cox B, Brown W J and Wax A 2018 *Biomed. Opt. Express* **9** 1232

[14] Kaur M, Lane P M and Menon C 2021 *Sensors* **21** 1–39

[15] Schulz-Hildebrandt H *et al* 2018 *Opt. Lett.* **43** 4386

[16] Kretschmer S, Jäger J, Vilches S and Ataman Ç 2018 *J. Micromech. Microeng.* **28** 1–9

[17] Shah R N, Kretschmer S, Nehlich J, Ataman C and Zappe H 2019 Compact OCT probe for flexible endoscopy enabled by piezoelectric scanning of a fiber/lens assembly *SPIE OPTO* (*San Francisco, USA*) p 10

[18] González-Cerdas G E, Stein P, Kretschmer S, Bauer C, Sandic D, Ataman C and Zappe H 2020 Micro-structured glass probe for endoscopic Optical coherence tomography *Photonics Europe* vol 11359 (France: SPIE) p 113590I

[19] Gottmann J, Hermans M and Ortmann J 2013 *J. Laser Micro Nanoeng.* **8** 15–18

[20] Choudhury D, Macdonald J R and Kar A K 2014 *Laser Photon. Rev.* **846** 827–46

[21] Georgescu D, Alexandrescu E, Mulţescu R and Geavlete B 2016 Chapter 1-cystoscopy and urinary bladder anatomy *Endoscopic Diagnosis and Treatment in Urinary Bladder Pathology* ed P A Geavlete (San Diego: Academic) pp 1–24

[22] Karl Storz SE KG 2015 Urology retrieved on 2021-04-20 through customer service (available at: http://www.karlstorz.com/cps/rde/xbcr/karlstorz_assets/ASSETS/3343855.pdf)

[23] Miodoński A J and Litwin J A 1999 *Anatomical Rec.* **254** 375–81

[24] Seibel E J and Smithwick Q Y 2002 *Lasers Surg. Med.* **30** 177–83

[25] Huo L, Xi J, Wu Y and Li X 2010 *Opt. Express* **18** 14375

[26] Vilches S, Kretschmer S, Ataman C and Zappe H 2017 *J. Micromech. Microeng.* **27** 105015

[27] Ginner L, Blatter C, Fechtig D, Schmoll T, Gröschl M and Leitgeb R A 2014 *Photonics* **1** 369–79

[28] Boreman G D 2001 *Modulation Transfer Function in Optical and Electro-Optical Systems* 1st edn (Bellingham: SPIE)

[29] Virtanen P *et al* 2020 *Nat. Methods* **17** 261–72

[30] Joseph J, Faiz K P, Lahrberg M, Tinguely J C and Ahluwalia B S 2020 *J. Phys. D: Appl. Phys.* **53** 044006